# ALGORITHMS AND SOFTWARE FOR GEOMETRIC MODELING OF THE IMAGE OF RETINAL VASCULAR SYSTEMS

***Ibodullayeva Feruza Uralovna***
*Samarkand branch of TATU named after Muhammad al-Khorazmi*
*Direction of computer systems in medicine 1st year student*

**Abstract** – The methods developed in recent years for synthesising an ocular fundus can be been divided into two main categories. The first category of methods involves the development of an anatomical model of the eye, where artificial images are generated using appropriate parameters for modelling the vascular networks and fundus. The second type of method has been made possible by the development of deep learning techniques and improvements in the performance of hardware (especially graphics cards equipped with a large number of cores).

**Keywords:** Fundus image analysis Synthetic retinal image Data augmentation Statistical features Predictive evaluation diseases

## Introduction

The analysis of retinal vascular microphotographs has a predominant role in clinical ophthalmology. However, there are few public domain high-resolution retinal images with handmade ground truth, especially those showing the classification of arteries and veins by ex pert physicians. A valid alternative is the creation of photorealistic images, with the possibility to specify peculiar characteristics that identify specific pathologies. This approach would not only allow the development and comparison of new automatic processing techniques but could also be useful in the predictive study of the evolution of diseases. A computer-aided diagnosis system for premature retinopathy was presented in [1]. It identifies a set of features that can be used to check for diseases of the fundus. Some of these can be extracted automatically and set as morphometric data (width, length, density, crossings, end-branch, and tortuosity). This automatic approach makes the system effective for non-physician graders. The framework proposed in this paper applies the principle of least action to generate the vascular tree on a simulated retinal image. Despite the simplicity of this approach, the algorithm has been successfully validated by comparing the results to statistical data from real datasets. This method is computationally fast, and a graphical interface allows the user to modify, if necessary, the characteristics of the vessels, and even to simulate possible pathologies. Considering the small number of datasets with retinal microphotographs in the public domain, this methodology could produce large archives of images as benchmarks for future segmentation and classification algorithms. A further possible application of this framework is data augmentation, which would be useful for training neural networks and generative adversarial networks.

In [2] the authors reviewed the literature on retinal image analysis, providing a wide range of topics and principles on which digital retinal image analysis is based, including image acquisition and processing, the automated segmentation and detection of retinal landmarks, vessel monitoring, morphological processing, the automatic

detection of pathology, quantitative measurements in ocular fundus images, and the reliability of quantitative measurements. A multiwavelet technique to segment the bottom portion of the eye without any pre-processing steps was presented contributions highlighted the correlation between coronary heart disease and coronary microvascular dysfunction [4]. An approach based on fractal analysis was reported in [5], which had the main objective of examining retinal vessels to find correlations between blood vessel features and coronary heart disease. The vascular network can be represented on the basis of the skeleton of the available segmented vessels and using a non-direct graph [6]. Image processing techniques for the detection, segmentation, tracking, and measurement of the widths of major temporal arcades, which used Gabor filters, were developed in [7]. A methodology for automated blood vessel extraction based on high-level local autocorrelation was described in [8]. An artificial neural network was used to classify the vessels in the fundus and a second neural network using Gabor filters was adopted to improve the overall performance. Some methods have been based on geometric models, and those based on a tubular shape have aroused a fair consensus within the scientific community [9]. However, because it is often necessary to manually adjust the parameters, these methods cannot be considered fully automatic. In other cases, an initial training must be performed to produce supervised methods, which seem to be strictly dependent on the values set by the user. A promising approach based on keypoints [10] was described in [11]. Regarding the study of the optic disc, a circular luminous object was proposed in [12] to define the unique round structure. In [13] a ridge detector was presented that used a retinal structure created by specialists that was simultaneously invariant to rotation, scaling, and curvature. This method included "context model" filters learned at multiple intervals. The tubularity measurements of these models were obtained by convolving a retinal image with a bank of second-order directional derivative filters. To cope with irregular and punctual structures, the authors generated a subset of elongated kernels, similar to a Gabor filterbank [14]. To mitigate the necessary efforts of this approach, an unsupervised methodology based on the wavelet algorithm "à trous" was adopted in [15]. Compared to an analysis using the standard Gabor function, this last methodology was based on a sequence of Gaussian filters, which were fast and effective for detecting the directions of the vessels. The result was a useful tool for quantifying the local tortuosity. The work was based on a pre-compiled bank of Gaussian elliptical filters and an algorithm [13] that allowed the direct comparison of the results obtained with those contained in the well-known digital retinal images for vessel extraction (DRIVE) [16] and DIARETDB01 [17] datasets. All of these studies were specifically concerned with the extraction of characterisations from retinal images. Similar techniques were used in the present study to verify the goodness of the proposed approach.

The DRIVE dataset [16] contains retinal images with and without pathologies (Fig. 1,top). It consists of 40 retinal images with a resolution of 768 × 584 pixels, including 33 that do not show any signs of diabetic retinopathy and 7 showing mild early diabetic retinopathy. The whole set is publicly available and divided into two sets for testing and training purposes. Manual classifications of the vessels as veins and arteries are available, and their morphometric characteristics were used to measure the ground truth as described in [26].

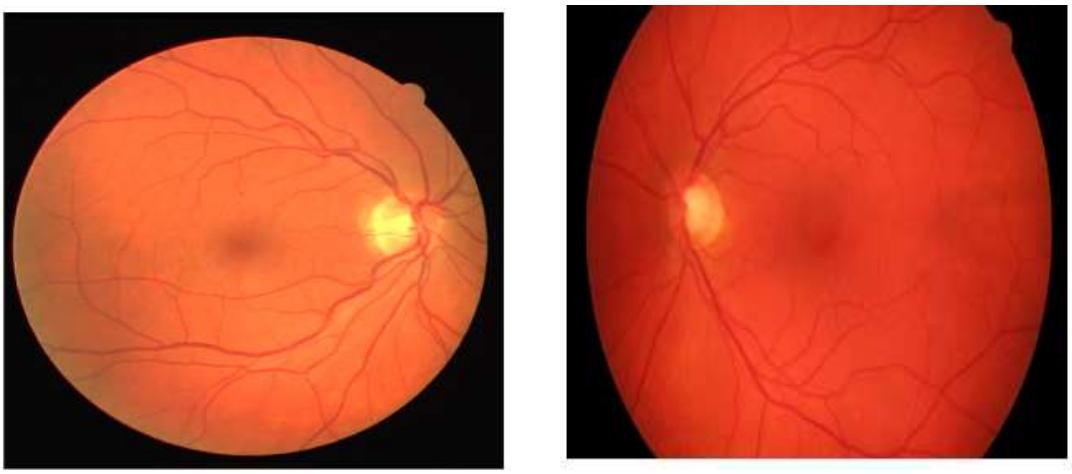

*Fig. 1. Images #2 and #8 from DRIVE and HRF datasets, respectively*

The HRF dataset The HRF image dataset [27,28] was created to support comparative studies of automatic segmentation algorithms for retinal bottom images. The size of the photographs is 2336 ×3504 pixels (Fig. 1,bottom). This public dataset currently contains 15 images of healthy patients, 15 images of patients with diabetic retinopathy, and

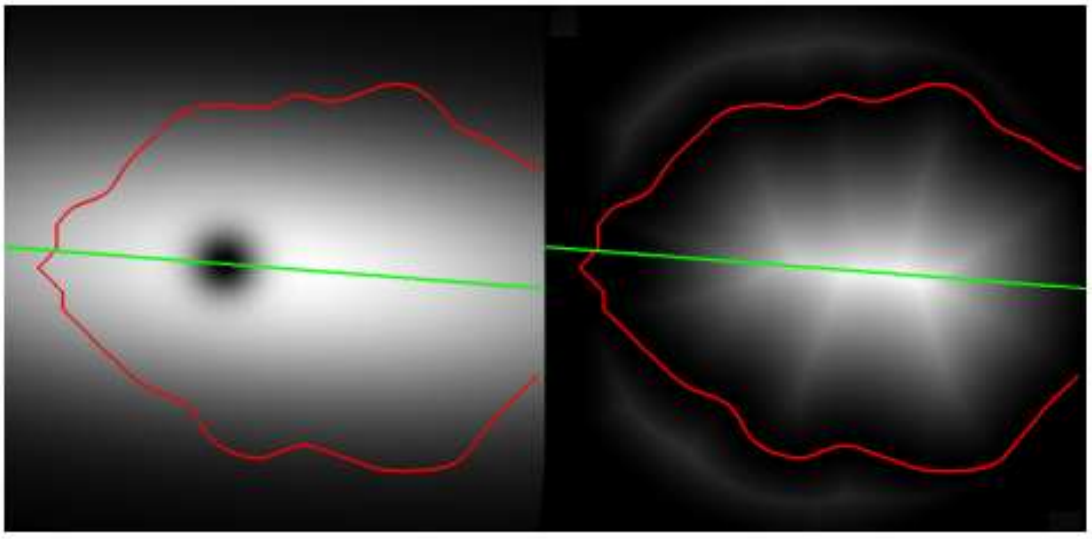

*Fig. 2. Major temporal arcade (red) with main axis indicated in green. The probability maps are created via two Gaussian functions (left) and the distance map (right). The grey level is proportional to the probability of choosing an endpoint. (For interpretation of the references to color in this figure legend, the reader is referred to the web version of this article.*

15 images of glaucomatous patients. Partial binary segmentations of the vessels (i.e. sometimes the finer details have been omitted) are provided for each image; these segmentations were generated by experts working in the field of retinal image analysis in collaboration with a group of ophthalmology clinicians. To the best of our knowledge there are no manual classifications of veins and arteries for this dataset.

A study of the main morphometric properties of the retina made it possible to verify the correctness of the approach proposed in this paper and its robustness with

respect to real microphotographs. Because arteries and veins have different information, the method can simply be calibrated for each of these two types of blood vessels, and then the resulting images can be combined together in a realistic way. For both vascular networks, inspiration was taken from the parabolic model described in [29] to reproduce the major temporal arcade (MTA). Without loss of generality, the simulated images were created assuming the optic disk was always on the left of the figure. The first step of this methodology was based on two main factors: the randomness in the choice of the end points of the vessels and the ramification of the vascular tree. Positioning the endpoints according to a purely random uniform distribution does not produce satisfactory results because a large number of small vessels should be placed in the area of the macula to allow a higher blood volume. The underlying idea of the proposed methodology was based on the application of the principle of least action and consequently of all the physics governing the nature of things. A purely intuitive and empirical, though reasonable, statement of this principle is that "among the various possibilities of inanimate motion, nature always chooses the most advantageous path". An easy though effective manner to place the endpoints is based on a probability map created from two Gaussian distributions and a Voronoi distance map. The first step is to compute an elliptical Gaussian distribution, centred on the area of the macula and oriented according to the MTA: the orientation of the Gaussian ellipsis is taken as the second order moment of the binary image that contains only the MTA.

It was experimentally verified that a good choice for the width of the Gaussian function is given by $\sigma_y = 3\sigma_y$ . Moreover, to exclude endpoints exactly at the fovea, another circular Gaussian map, centred on the fovea and with sigma equal to the presumed size of the fovea itself, is subtracted (Fig. 2, left). All these settings can be adjusted according to the size of the image to be created.

The proposed method prevented this side effect via the Catmull–Rom interpolation [33]. Informally, this is a special case of cardinal splines. These in turn are derived from the cubic Hermite splines, which are typically used to interpolate numerical data to obtain a smooth continuous function. The cardinal spline overcomes the main disadvantages of cubic splines, namely the lack of local control and the need to solve a large system of linear equations. In order to generate a feasible central line for the retinal vessel, four control points are necessary to determine the overall course. In this specific case, starting and ending points $P_1$ and $P_2$ and two further random points $P_3$ and $P_4$ are placed close to the segment between $P_1$ and $P_2$. Their positions are randomly identified within double Gaussian functions, centred at one third and two thirds of that segment and with a standard deviation equal to one (Fig. 3, left). When using the same standard deviation value on both sides of the vessel, this will oscillate and be basically straight; however, it is possible to obtain a vessel that tends towards the right (left) by slightly increasing the Gaussian width on the right (left). The four points ensure sufficient variability among the vessels, whose overall appearance (e.g. tortuosity) can be controlled through the width of these Gaussian functions. Obviously, these four points are not sufficient to draw a realistic vessel. Therefore, additional control points are added in somewhat random positions, roughly equally spaced, similar to $P_3$ and $P_4$ (Fig. 3, right). All these points are then interpolated to produce the

centerline through the polynomial

$$\mathbf{P}(t) = s(-t^3 + 2t^2 - t)\mathbf{P}_1 + s(-t^3 + t^2)\mathbf{P}_2 + (2t^3 - 3t^2 + 1)\mathbf{P}_2 + s(t^3 - 2t^2 + t)\mathbf{P}_3 + (-2t^3 + 3t^2)\mathbf{P}_3 + s(t^3 - t^2)\mathbf{P}_4 \quad (1)$$

with $\mathbf{0 \le t \le 1.}$

This formula describes the parabola between $P_1$ $P_3$ , and $P_4$, the parabola between $P_3$ $P_4$ , and $P_2$, the linear combination of the

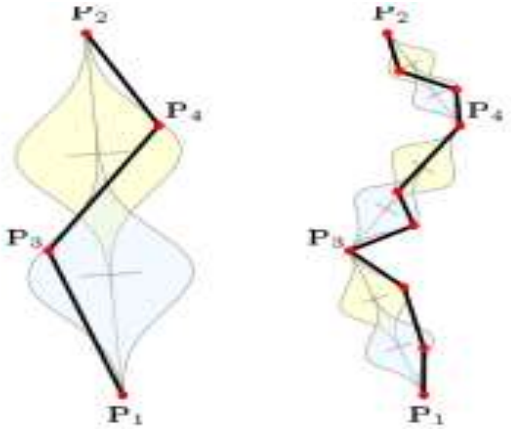


Fig. 3. Starting from P1 and $P_2$ $P_3$, and $P_4$ are added within normal probability density function (in blue and yellow, respectively). Further control points are added to perturb the initial coarse centreline. (For interpretation of the references to color in this figure legend, the reader is referred to the web version of this article.).

parabolas between $P_3$ and $P_4$. These individual parts connect smoothly (i.e. the first derivatives are equal at each point). Tension parameter $T = 1\text{-}2_s$ makes it possible to modify the curve, where a negative value causes loops in the space between the control points, while a positive tension wraps the interpolated curve around them.

For T = 1 the polynomial becomes

$$\mathbf{P}(t) = (3t^2 - 2t^3)(\mathbf{P}_3 - \mathbf{P}_2) + \mathbf{P}_2$$

which is the straight line from $\mathbf{P}_2$ to $\mathbf{P}_3$.

For $T = 0$ the polynomial becomes

$$\mathbf{P}(t) = (-0.5t^3 + t^2 - 0.5t)\mathbf{P}_1 + (1.5t^3 - 2.5t^2 + 1)\mathbf{P}_2 + (-1.5t^3 + 2t^2 + 0.5t)\mathbf{P}_3 + (0.5t^3 - 0.5t^2)\mathbf{P}_4 \quad (2)$$

which corresponds to the so-called Catmull-Rom.

Each time a complete vessel is added, the entire probability map must be updated: the number of iterations depends on the resolution of the synthetic image. In any case, the fovea is avoided by using the map described in Section 2.3 (Fig. 2,). In order to make the vessels so far generated more realistic, it is also necessary to consider the calibre, which decreases linearly as it moves away from the optic disc. The statistical and physiological indications that distinguish arteries from veins have also been taken into account for this feature. At the same distance from the optic disc, the arteries are generally slightly larger than the veins. In addition, vessels in direct contact with the

optic disc but which have a significantly shorter length than the major temporal arcade are assigned a very small calibre. Further realism is given by the randomness with which the larger vessels connect to the main ones: with the upper limit of the main calibre, the secondary vessels can sometimes appear much thinner. Once the appropriate calibre is associated with each point of the centreline, a colour profile is applied, which is resized according to the calibre and orthogonal to the centreline. This profile, which was differentiated for veins and arteries, was created by analysing the real images in the dataset, and it also includes transparency to improve the superimposition of the vessels on the background fundus image. Moreover, the amount of opacity is proportional to the calibre itself. The overlapping of veins and arteries is observable in the real images; this is not admissible for vessels of the same type. However, in order to prevent a vein and an artery from intertwining in an unnatural way, the passage of the veins over the arteries (and vice versa) is force to be globally, not locally, random. That is, all the overlaps between vessels are labelled as vein-on-artery or artery-on-vein; then these labels are updated so that they are locally all of the same type, chosen in a random way (Fig. 4).

The description of the framework highlights its interactive versatility both for the researcher and the clinician, who can use it to evaluate possible emerging pathologies. The association between different biomarkers of the retina and cerebrovascular diseases has been widely studied in the literature. Cerebrovascular diseases (e.g. clinical stroke, silent cerebral infarction, and cerebral haemorrhage) are identified with numerous causes of death. Consequently, the retina, which is considered to be an extension of the brain, shares the brain's vascular malformations. A medical researcher, supported by this system, will be able to manipulate control points in order to synthesise pathologies characterised by anomalies in vessel parameters such as the length, calibre and distances, tortuosity, curvature and sum of angles, presence of consecutive curvatures, and inflection countermeasure [35].

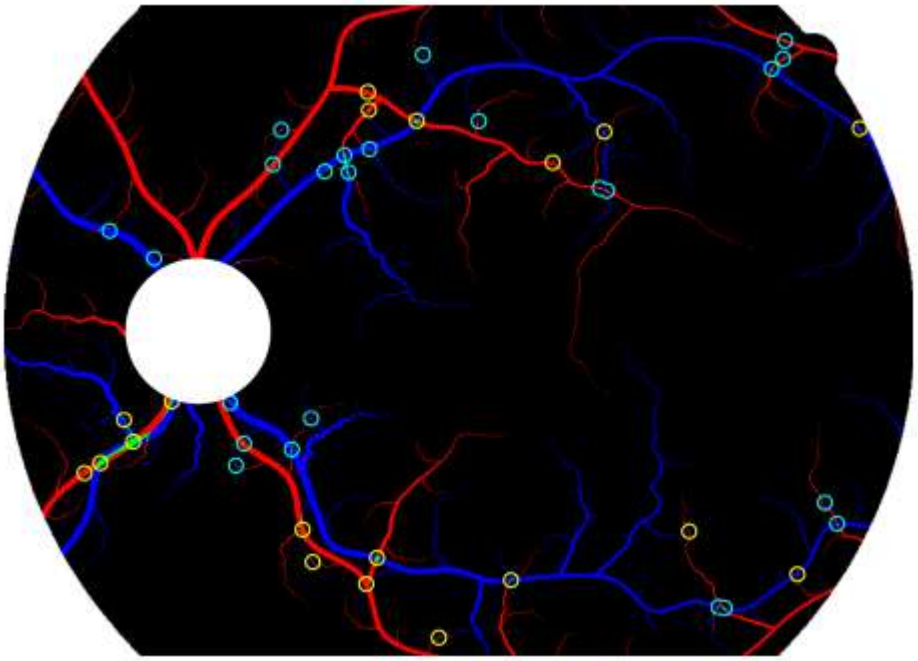

Fig. 4. Application of the profiles of  on the calibers of . The circles indicate the overlapping vein-on-artery (cyan) or artery-on-vein (yellow). Locally, these circles

show the same color. The reader is referred to the electronic version of the article for interpretation of the colours. in this figure.

As a result, a clinical physician can study these variations applied to an image rendered in a specific moment of time, to predict in detail the degenerative consequences. For example, a reduction in vessel oxygenation implies an increase in blood flow, as well as an increase in the tortuosity of peripheral vessels. Therefore, the tortuosity, lack of oxygenation, and changes in the muscle tone of the vessel walls (i.e. thickness) may indicate possible pathologies such as ischemic optic neuropathy, neovascularisation, and retinal vein occlusion. An analysis of markers extracted from synthetic images will allow a detailed study that will assist a clinical doctor to improve their understanding of the mechanisms that lead to morphological changes in the vascularisation of the retina and consequently the cerebrovascular system. The GUI capabilities allow for easy image manipulation and are an interesting utility for identifying innovative vascular properties for disease characterisation. For example, synthetic retinal images with simulated vascular obstructions can be suggested as surrogate markers in a stroke risk study. This will provide support for identifying those patients who tend to have disease progression in their central nervous system.

## References:


1. K. Nisha, G. Sreelekha, P. Sathidevi, P. Mohanachandran, A. Vinekar, A computeraided diagnosis system for plus disease in retinopathy of prematurity with structure adaptive segmentation and vessel based features, Comput. Med. Imaging Graph. 74 (2019) 72–94.
2. N. Patton, T. Aslam, T. MacGillivray, I. Deary, B. Dhillon, R. Eikelboom, K. Yogesan, I. Constable, Retinal image analysis: Concepts, applications and potential, Prog. Retin. Eye Res. 25 (1) (2006) 99–127.
3. Y. Wang, G. Ji, P. Lin, E. Trucco, Retinal vessel segmentation using multiwavelet kernels and multiscale hierarchical decomposition, Pattern. Recognit. 46 (8) (2013) 2117–2133.
4. B. McClintic, J. McClintic, J. Bisognano, R. Block, The relationship between retinal microvascular abnormalities and coronary heart disease: a review, Am. J. Med. 123 (4) (2010) 1–7.
5. G. Liew, P. Mitchell, E. Rochtchina, T. Wong, W. Hsu, M. Lee, A. Wainwright, J. Wang, Fractal analysis of retinal microvasculature and coronary heart disease mortality, Eur. Heart J. 32 (4) (2011) 422–429.
6. C. Lupascu, D. Tegolo, Graph-based minimal path tracking in the skeleton of the retinal vascular network, IEEE Symposium on Computer-Based Medical Systems, 2012.
7. F. Oloumi, R. Rangayyan, P. Casti, A. Ells, Computer-aided diagnosis of plus disease via measurement of vessel thickness in retinal fundus images of preterm infants, Comput. Biol. Med. 66 (2015) 316–329.
8. J. Tan, U. Acharya, K. Chua, C. Cheng, A. Laude, Automated extraction of retinal vasculature, Med. Phys. 43 (5) (2016) 2311–2322.
9. R. Annunziata, A. Kheirkhah, S. Aggarwal, P. Hamrah, E. Trucco, A fully automated Fig. 15. Graphic representation of all endpoints in DRIVE (grey) and

in the simulated images (green). The excluded regions are due to the fovea and macula; their positions do not coincide in the images because they depend on the particular background image we used. The reader is referred to the electronic version of the article for interpretation of the colours in this figure. D. Lo Castro, et al. Journal of Biomedical Informatics 108 (2020) 103490 11 tortuosity quantification system with application to corneal nerve fibres in confocal microscopy images, Med. Image Anal. 32 (2016) 216–232.

10. F. Bellavia, D. Tegolo, C. Valenti, Keypoint descriptor matching with context-based orientation estimation, Image Vis. Comput. 32 (8) (2014) 559–567.
11. L. Zhanga, M. Fisherb, W. Wang, Retinal vessel segmentation using multi-scale textons derived from keypoints, Comput. Med. Imaging Graph. 45 (2015) 47–56.
12. S. Lu, J. Lim, Automatic optic disc detection from retinal images by a line operator, IEEE Trans. Biomed. Eng. 58 (1) (2011) 88–94.
13. R. Annunziata, E. Trucco, Accelerating convolutional sparse coding for curvilinear structures segmentation by refining SCIRD-TS filter banks, IEEE Trans. Med. Imag. 35 (11) (2016) 2381–2392.
14. D. Lo Castro, D. Tegolo, C. Valenti, Filter bank: a directional approach for retinal vessel segmentation, in: 10th International Congress on Image and Signal Processing, BioMedical Engineering and Informatics, 2018, pp. 1–6.
15. D. Lo Castro, D. Tegolo, C. Valenti, A fast multiresolution approach useful for retinal image segmentation, 7th International Conference on Pattern Recognition Applications and Methods, 2018, pp. 340–345.
16. DRIVE, https://www.isi.uu.nl/Research/Databases/DRIVE.
17. DIARETDB1, https://www.it.lut.fi/project/imageret/diaretdb1.
18. S. Aghamirmohammadali, R. Bozorgmehry Boozarjomehry, M. Abdekhodaie, Modelling of retinal vasculature based on genetically tuned parametric L-system, R. Soc. Open Sci. 5 (5) (2018).
19. X. Liu, H. Liu, A. Hao, Q. Zhao, Simulation of blood vessels for surgery simulators, International Conference on Machine Vision and Human-machine Interface, 2010, pp. 377–380.
20. M. Kocinski, A. Klepaczko, A. Materka, M. Chekenya, A. Lundervold, 3D image texture analysis of simulated and real-world vascular trees, Comput. Methods Programs Biomed. 107 (2) (2012) 140–154.
21. S. Fiorini, M.D. Biasi, L. Ballerini, E. Trucco, A. Ruggeri, Automatic Generation of Synthetic Retinal Fundus Images, in: Smart Tools and Apps for Graphics - Eurographics Italian Chapter Conference, 2014, pp. 41–4.
22. P. Costa, A. Galdran, M. Meyer, M. Niemeijer, M. Abràmoff, A. Mendonça, A. Campilho, End-to-end adversarial retinal image synthesis, IEEE Trans. Med. Imaging 37 (3) (2018) 781–791.
23. J.T. Guibas, T.S. Virdi, P.S. Li, Synthetic medical images from dual generative adversarial networks, 31st Conference on Neural Information Processing Systems, 2017.
24. H. Zhao, H. Li, S. Maurer-Stroh, L. Cheng, Synthesizing retinal and neuronal images with generative adversarial nets, Med. Image Anal. 49 (2018) 14–26.

25. M. Kretowski, Y. Rolland, J. Bèzy-Wendling, J.-L. Coatrieux, Fast algorithm for 3D vascular tree modeling, Comput. Methods Programs Biomed. 70 (2) (2003) 129–136.
26. J.T. Guibas, T.S. Virdi, P.S. Li, A manually-labeled, artery/vein classified benchmark for the DRIVE dataset, IEEE Symposium on Computer-Based Medical Systems, 2013, pp. 485–488.
27. A. Budai, R. Bock, A. Maier, J. Hornegger, G. Michelson, Robust vessel segmentation in fundus images, Int. J. Biomed. Imaging 2013 (2013).
28. HRF, https://www5.cs.fau.de/research/data/fundus-images.
29. F. Oloumi, R. Rangayyan, A. Ells, Parabolic modeling of the major temporal arcade in retinal fundus images, T. Instrum. Meas. 61 (7) (2012) 1825–1838.
30. M. Manduhu, M. Jones, A work efficient parallel algorithm for exact Euclidean distance transform, IEEE Trans. Image Process. 28 (11) (2019) 5322–5335.
31. H. Hamad, D. Tegolo, C. Valenti, Automatic detection and classification of retinal vascular landmarks, Image Anal. Stereol. 33 (13) (2014) 189–200.
32. G. Hichem, F. Chouchene, H. Belmabrouk, 3d model reconstruction of blood vessels in the retina with tubular structure, Int. J. Electr. Eng. Informat. 7 (4) (2015) 724–734.
33. D. Salomon, The Computer Graphics Manual, Springer, 2011.
34. O. Gambino, R. Pirrone, S. Vitabile, L. Rundo, A framework for data-driven adaptive GUI generation based on DICOM, J. Biomed. Inform. 88 (2018) 37–52.
35. S. Ciurica, M. Lopez-Sublet, B. Loeys, I. Radhouani, N. Natarajan, M. Vikkula, A. Maas, D. Adlam, A. Persu, Arterial tortuosity: Novel implications for an old phenotype, Hypertension 73 (5) (2019) 951–960